*Title

Analysis of pressurized operation of 10 layer solid oxide electrolysis stacks

*Author names and affiliations

M. Riedel*, M. P. Heddrich, K. A. Friedrich

German Aerospace Center (DLR), Institute for Engineering Thermodynamics, Pfaffenwaldring 38-40, 70569, Stuttgart, Germany

*Corresponding author: Marc.Riedel@dlr.de

Abstract

High temperature steam electrolysis using solid oxide electrolysis cell (SOEC) technology can provide hydrogen as fuel for transport or as base chemical for chemical or pharmaceutical industry. SOECs offer a great potential for high efficiencies due to low overpotentials and the possibility for waste heat use for water evaporation. For many industrial applications hydrogen has to be pressurized before being used or stored. Pressurized operation of SOECs can provide benefits on both cell and system level, due to enhanced electrode kinetics and downstream process requirements. Experimental results of water electrolysis in a pressurized SOEC stack consisting of 10 electrolyte supported cells are presented in this paper. The pressure ranges from 1.4 to 8 bar. Steady-state and dynamically recorded U(i)-curves as well as electrochemical impedance spectroscopy (EIS) were carried out to evaluate the performance of the stack under pressurized conditions. Furthermore a long-term test over 1000 hours at 1.4 bar was performed to evaluate the degradation in exothermic steam electrolysis mode. It was observed that the open circuit voltage increases with higher pressure due to well-known thermodynamic relations. No increase of the limiting current density was observed with elevated pressure for the ESC-stacks (electrolyte supported cell) that were investigated in this study. The overall and the activation impedance were found to decrease slightly with higher pressure. Within the impedance studies, the ohmic resistance

was found to be the most dominant part of the entire cell resistance of the studied electrolyte supported cells of the stack. A constant current degradation test over 1000 hours at 1.4 bar with a second stack showed a voltage degradation rate of 0.56 %/kh.

Keywords

Solid oxide electrolysis, pressurized SOEC, pressure, stack, electrolysis

1. Introduction

Solid Oxide Electrolysis Cells (SOECs) offer a great potential for a highly efficient conversion of renewable electrical energy and the production of fuels for mobility or commodity chemicals for chemical and pharmaceutical industry. High temperature steam electrolysis (HTSE) using SOECs can therefore function as a key technology for sector coupled energy storage systems. The high operating temperature of SOECs leads to reduced electrochemical losses, fast kinetics and offers the option to use waste heat [1]. Hydrogen, as the product of the HTSE is arguably a versatile, efficient and environmentally friendly fuel [2], [3]. It can be stored under pressure in gas tanks, injected into the natural gas grid or can further be used directly as a commodity chemical for industrial processes. The operation of the HTSE under elevated pressure offers several benefits. Costs for auxiliary components like compressors for the pressurization of the produced hydrogen in HTSE systems can be omitted or reduced. Furthermore, the operation of the HTSE under elevated pressure has already been published to be energetically even more efficient for fuel electrode supported cells [4]–[8]. In most of the reported studies single cells have been tested for electrolysis performance and durability under elevated pressure. However, only a limited number of studies focus on the performance of stacks in HTSE mode [9]–[11].

In this study experimental data of commercially available 10-layer planar stacks with electrolyte supported cells operated at pressures ranging from 1.4 to 8 bar in steam electrolysis mode is presented. Steady-state and dynamically recorded U(i)-curves were performed, as well as electrochemical impedance spectroscopy (EIS) to investigate the pressure effect in more detail. A long-term test over 1000 hours at 1.4 bar was furthermore performed to investigate the durability of the stack during steam electrolysis operation.

2. Test setup

The pressurized SOC stack test facility at DLR is shown in Figure 1. The experimental test setup offers the opportunity to characterize short stacks in SOEC as well as in SOFC mode in an absolute pressure range between 1.4 and 8 bar. The stack is placed inside a furnace that is installed inside a

pressure vessel. During operation the whole setup is pressurized. The pressurization can be conducted with a maximum speed of 1 bar/100 min. The temperature range for the experimental investigations is between 650 and 950 °C. On the fuel side gases like H_2, N_2, He, CH_4, CO and CO_2 can be supplied. Furthermore the test rig offers a stable steam supply for the fuel feed of up to 100 %. For the oxygen electrodes air, N_2 and O_2 are available. All gases are controlled by mass flow controllers and preheated via an electric heater before entering the stack. The temperature of the preheater can be controlled independently from the furnace temperature.

Figure 1: Pressurized SOC stack test facility of DLR.

A challenge in the operation of SOC stacks on elevated pressure is to keep the pressure differences between anode and cathode gas compartment and the surrounding furnace atmosphere constantly very low (< 20 mbar). Since a large pressure difference may lead to the destruction of the whole stack, all pressures are controlled by a sensitive differential pressure control system of the test rig. The differential pressures between fuel side/air side and air side/vessel are measured at the outlet pipes of the three gas compartments. To enable the precise pressure control, the gas volume of the stack is balanced by equalizing tanks (500 l each) at the anode and cathode outlet to match the furnace volume. Three independently controlled valves for the gas volumes of the two equalizing tanks and the pressure vessel are installed to maintain the set pressure differences between all gas compartments. The released gases are combusted in an off-gas burner. Further information about the setup operated in fuel cell mode are given in [12].

As well as the possibility to record current-voltage characteristics of the stack and of its individual cells, the test rig offers the opportunity to perform impedance spectroscopy during operation. For determining the gas compositions of the in- and outlet streams a gas analysis system is available. Since the investigated stacks have an open oxygen electrode design and pure oxygen with its corrosive characteristic is produced during electrolysis, oxygen gas compartment had to be decoupled from the furnace environment to prevent oxidation of the furnace components. Furthermore, in case of a leakage between anode and cathode gas compartment, reactants would stream into the furnace unimpededly and may force oxidation or electric short circuits in the test rig. Due to these aspects, the stack is housed in a gastight steel box with internal gas manifolding (Figure 2). The necessary compression force is supplied to the stack through a thin transfer metal sheet on the top of the box. Current collectors and voltage wires are lead through the stack box to the designated connection points of the test rig. For measuring the temperatures inside the stack during operation, five thermocouples are placed directly on the oxygen electrodes of the stack. This offers the possibility for an accurate temperature measurement and an investigation of the temperature profile in the stack during operation. One thermocouple is placed on layer one and ten respectively. The three remaining thermocouples are placed at quarter, half and three-fourths of the length of the middle cell of the stack.

(a) (b)

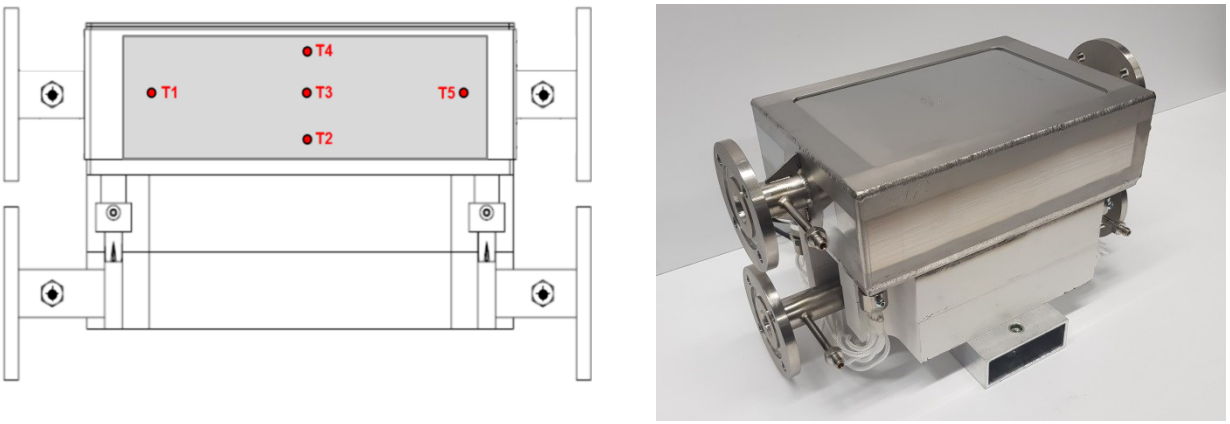

Figure 2: (a) Sketch of the steel box with the implemented 10 layer stack and positioning of the five thermocouples. (b) Photo of one manufactured stack box at the beginning of the study.

The commercially available planar stacks used in this study are co-flow setups and contain 10 electrolyte supported cells, each with an active area of 127.8 cm^2. Each cell consists of an approximately 55 µm thick lanthanum strontium cobalt ferrite oxide (LSCF) as oxygen electrode, a 90 µm thick 3 mol% yttria-stabilized zirconia (3YSZ) as electrolyte, gadolinia-doped ceria layer (GDC) between electrolyte/fuel electrode and electrolyte/air electrode, and a 30 µm thick nickel gadolinia-doped ceria (Ni-GDC) as fuel electrode.

3. Experimental Methodology

In this study steady-state as well as dynamically recorded current-voltage curves were performed for characterizing the stacks under pressurized operation in steam electrolysis mode. For steady-state U(i)-curves, current density was increased stepwise by 39.12 $mA \cdot cm^{-2}$ for every measuring point. The gas flows with a composition of 90 % H_2O and 10 % H_2 were adjusted at every current density point for a constant steam conversion rate (RC) of 60 % at the cells. A flux of 10 slpm air was supplied to the stack on the anode side. Reaching stationary conditions in the stack took at least 90 minutes depending on operating point. Afterwards cell voltages and temperatures were logged and the experimental parameters were switched to the next measuring point with a higher current density. Due to this method it is possible to record a U(i)-characteristic with a current density dependent temperature profile at a constant steam conversion rate.

In contrast to that, dynamically recorded U(i)-curves were performed with a fast increase of current density of $1.96 \cdot 10^{-3}$ $A \cdot cm^{-2} \cdot s^{-1}$. The gas flows were defined for a steam conversion rate of 60 % at 0.8 $A \cdot cm^{-2}$. Air with 10 slpm was supplied to the anode side of the stack. Due to the fast current ramp a quasi-isothermally recorded U(i)-curve with a very small temperature change over the complete range of current density could be performed.

Electrochemical impedance analysis was performed galvanostatically with a Zahner Zennium at $7.8 \cdot 10^{-3}$ $A \cdot cm^{-2}$ with an AC amplitude of 0.38 A. The applied current density leads to a voltage which is very close to OCV at the studied conditions and ensures measuring in pure electrolysis mode.

The frequency range for impedance spectroscopy was defined to be in the range of 100 kHz to 50 mHz with single sine wave impedance.

4. Results and discussion

4.1. Steady-state U(i)-curves

Figure 3 shows the performed steady-state U(i)-curves at a furnace temperature of 800 °C and three different operating pressures of 1.4, 4 and 8 bar respectively. The showed voltage belongs to the middle cell of the stack. Additionally, the core temperature T3, which is assumed to be the characteristic stack temperature, and the theoretical Nernst voltage for every measuring point are plotted against current density. The recording of the U(i)-curves was aborted before the maximum stack temperature of 860 °C or cell voltages above 1.4 V were reached.

The Nernst voltage was calculated with the following equation by using the definition of the mole fraction $X_i = p_i/p_0$ and by assuming ideal gases ($a_i = p_i/p_0$).

$$U_{ideal} = U_0 + \frac{RT}{zF}\ln\left(\frac{X_{H2}\cdot X_{O2}^{0.5}}{X_{H2O}}\right) + \frac{RT}{2zF}\ln\left(\frac{p}{p_0}\right) \quad (1)$$

Considering the SOC stack to behave as a continuous stirred-tank reactor (CSTR), an averaged gas composition between inlet and outlet of the stack is taken as basis for the calculation of the temperature and conversion rate dependent Nernst voltage (U_{ideal}) [13]. Only at OCV conditions, the gas composition of the inlet is taken for calculating the theoretical values.

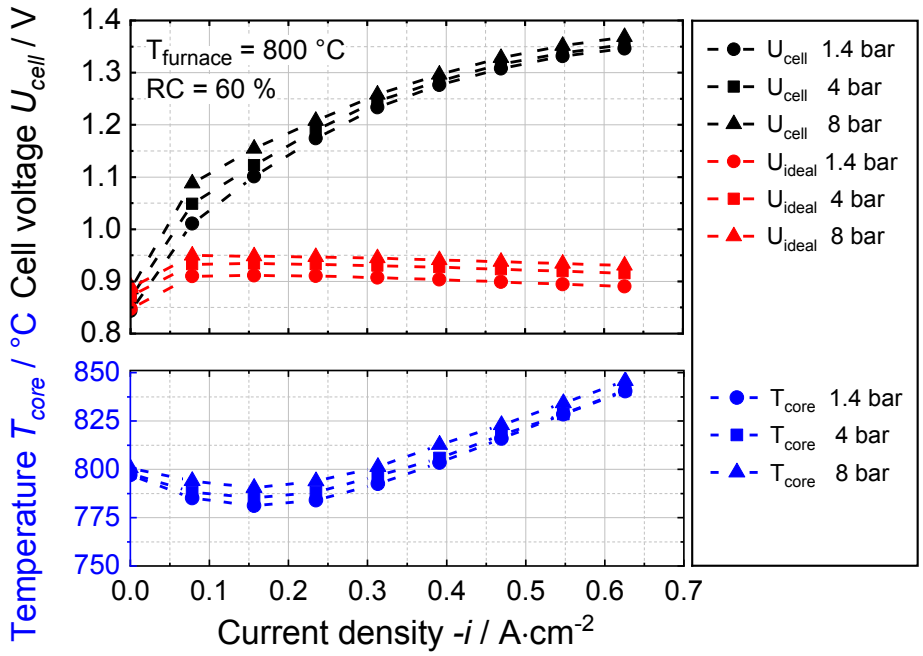

Figure 3: Steady-state U(i)-curves recorded with a 10-layer planar SOC stack at a furnace temperature of 800 °C, air and 90 % H_2O + 10 % H_2 with a constant steam conversion rate of 60 % at every measuring point.

As predicted by the Nernst equation, the open circuit voltage was found to increase with increasing operating pressure. The measured cell voltages of Figure 3 are in good agreement with the theoretical values, indicating an accurate water dosage and hardly any leakage in the stack.

The core temperature of the stack decreases at low current densities due to the endothermic water reduction reaction. At a voltage of 1.28 V for thermoneutral operation, the current density shows values of approximately -0.36 to -0.4 A·cm^{-2} depending on operating pressure. Due to the higher OCV and the low influence of kinetics on the stack performance at higher operating pressures, the current density for thermoneutral operation is decreased with higher pressure.

The measured core temperature T3 (characteristic stack temperature; see section 4.4) shows slightly higher values than the furnace temperature at thermoneutral operation. This behavior could possibly indicate that the thermocouple for the measurement of the core temperature at the middle length of cell 5 measures closer to a hotspot and may not be a well-chosen characteristic stack temperature within these experimental conditions. Nevertheless, the temperature deviation at the thermoneutral operating point between core of the stack and furnace temperature is only in the

range of 2 to 6 K. With higher current densities heat production increases due to the internal resistances of the cells and the stack shows an exothermic behavior.

In the range of low current densities, thermodynamics' influence on the stack and cell performance is bigger than the influence of electrochemical reactions' kinetics. The higher the current density becomes, the more ionic and electronic conduction, activation and diffusion resistances affect the cell performance. At elevated pressure, internal cell resistances are known to decrease due to superior mass transport and decreased diffusion overpotential. Due to this aspect, the impact of pressurization on cell performance becomes bigger with higher current densities. The U(i)-curves recorded at 4 and 8 bar show a slight decrease of the slope with higher current densities compared to the U(i)-curve recorded at 1.4 bar. Associated is a slight convergence of the U(i)-curves with higher current densities. Nevertheless a crossing of the U(i)-curves, as already reported in literature for fuel electrode supported cells, cannot be observed with the investigated electrolyte supported cell stack up to a cell voltage of 1.4 V and the investigated maximum operating pressure of 8 bar [4], [14], [15].

During the performed steady-state U(i)-curves, a distinct vertical and horizontal temperature profile forms within the stack. By means of the five thermocouples implemented on certain oxygen electrodes in the 10-layer stack, the temperature distribution depending on the operating point can be described. Figure 4 shows the current-dependent temperature profile and the voltage of cell 1, 3, 5, 7 and 10 of the stack during the 1.4 bar steady-state U(i)-curve shown in Figure 3.

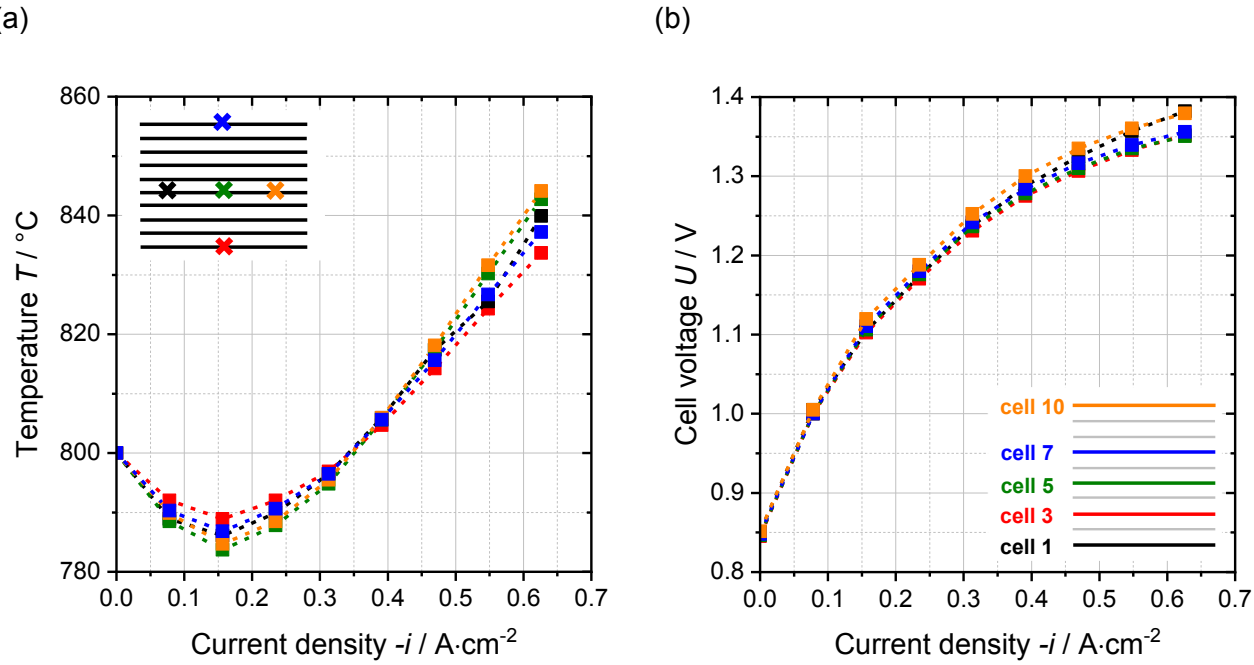

Figure 4: During the 1.4 bar steady-state U(i)-curve recorded (a) temperature distribution within the stack. The sensor location is indicated by the colored crosses. (b) shows the cell voltages of specific cells of the same experiment. The cells shown in the graph are indicated by colors.

The recorded temperatures show a maximum deviation of 5.2 K in the endothermic and 10.4 K in the exothermic operating mode. As expected, the surrounding furnace environment shows the most significant thermal influence on both outer layers of the stack. During endothermic operation both layers have the highest and in exothermic operation the lowest temperature. The temperatures measured along the length of layer 5 show a maximum deviation of 3 K, whereas the thermocouple close to the inlet recorded the lowest values. The temperature profile along the height of the stack leads to the inequality of the cell voltages shown in Figure 4 b. At high current densities the cell voltages show a maximum deviation of 31 mV. At the operating pressures of 4 and 8 bar, the described behavior of the temperatures and cell voltages were not observed to be significantly different. At 4 bar and 8 bar, a maximum temperature deviation of 4.9 K and 5.2 K in endothermic and 10.8 K and 9 K in the exothermic mode is determined. The cell voltages show a maximum deviation of 35 mV and 29 mV respectively.

4.2. Dynamically recorded U(i)-curves

Dynamically recorded U(i)-characteristics are shown in Figure 5 and Figure 6. Due to the already mentioned fast current ramp for the dynamically recorded U(i)-curves, only a small temperature deviation in the stack of less than 7 K was observed. The small temperature spread leads to a very low voltage deviation between all 10 cells of the stack. Therefore, the middle cell of the stack with the corresponding core temperature is shown in the following graphs. The voltage shows an almost linear behavior up to the defined maximum voltage of 1.4 V. The slope is slightly decreased with higher operating pressures, which is also indicated by the ASR values shown in the diagrams.

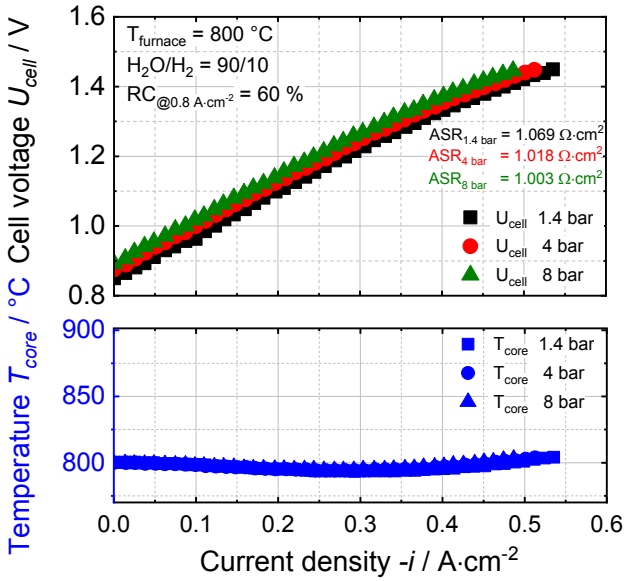

Figure 5: Dynamically recorded U(i)-curves at three different operating pressures, a furnace temperature of 800 °C, air and 90 % H_2O + 10 % H_2 with a steam conversion rate of 60 % at 0.8 A·cm^{-2}.

The ASR values are calculated by linearizing the U(i)-curves. Due to the fact that the conversion rate over the current density range is not constant, theoretical Nernst voltage is calculated with the actual current depending gas composition and the actual measured characteristic temperature for every measuring point. By subtracting the theoretical voltage from the measured voltage and dividing it by the current density, ASR values are obtained for every measuring point. The values shown in the diagram of Figure 5 are averaged values over the range of a current density from 0.1 to 0.45 A·cm^{-2}.

The diagrams in Figure 6 show two different U(i)-curves recorded at furnace temperatures of 750 °C and 850 °C respectively.

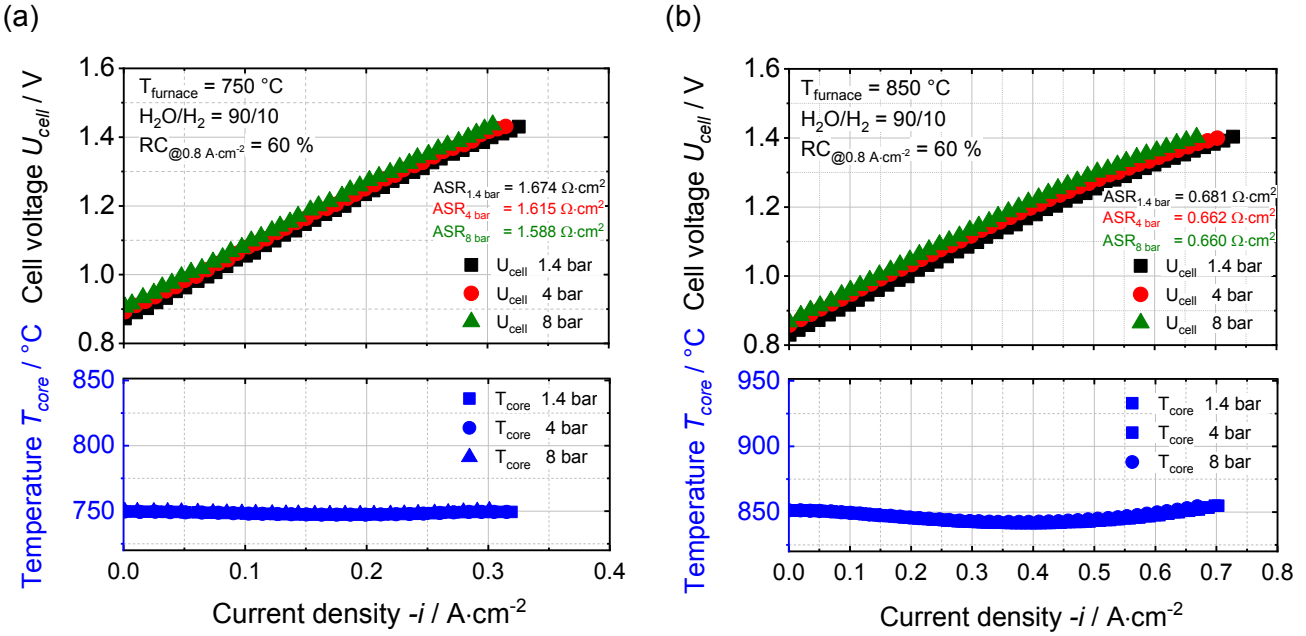

Figure 6: Dynamically recorded U(i)-curves at three different operating pressures, gas flows of air and 90 % H_2O + 10 % H_2 for a steam conversion rate of 60 % at 0.8 A·cm^{-2} and a furnace temperature of (a) 750 °C and (b) 850 °C.

The ASR values shown in diagram (a) are averaged over the range of a current density from 0.1 to 0.25 A·cm^{-2} and the values in diagram (b) over the range of 0.1 to 0.6 A·cm^{-2}. At all three operating temperatures shown in Figure 5 and Figure 6, no positive pressure effect on the achievable current density of the stack could be observed up to a cell voltage of 1.4 V and an operating pressure of up to 8 bar.

4.3. Investigation of the pressure effect via EIS

To investigate the pressure influence on the cell performance in more detail, impedance spectra were recorded at operating pressures of 1.4, 4 and 8 bar. As feed gas 1 slpm/cell with a composition of 90 % H_2O and 10 % H_2 was supplied to the stack. The anode side was flushed with 1 slpm/cell air. A small current density of 7.8·10^{-3} A·cm^{-2} was applied to the stack. Despite the applied small current, cell voltages remained very close to OCV at the studied conditions and recording of the spectra via single sine wave impedance in pure electrolysis mode was ensured.

The inset in Figure 7 shows the Nyquist plot of the three different impedance spectra. As can be seen, the ohmic resistance is not influenced by pressure and was found to be the most dominant part of entire cell resistance with 0.85 $\Omega \cdot cm^2$ at 800 °C. The total area specific resistance (ASR_{tot}) shows a very slight decrease with elevated pressures, which explains the already shown U(i)-characteristic with the slightly decreased slope at higher operating pressures. In the frequency dependent plot of Figure 7 a big resistance in the low frequency part of the spectra could be observed. This resistance is typically attributed to the gas concentration impedance, the coupled phenomena of gas conversion and gas diffusion. The peak frequency was found to decrease with higher pressures, which is in good agreement with already existing literature about pressurized operations of SOCs [16]. These findings state that as pressure increases, the number of gas molecules in the gas distribution layer and the fuel electrode increases and results in an increase of the gas conversion capacitance and therefore the decrease of the peak frequency.

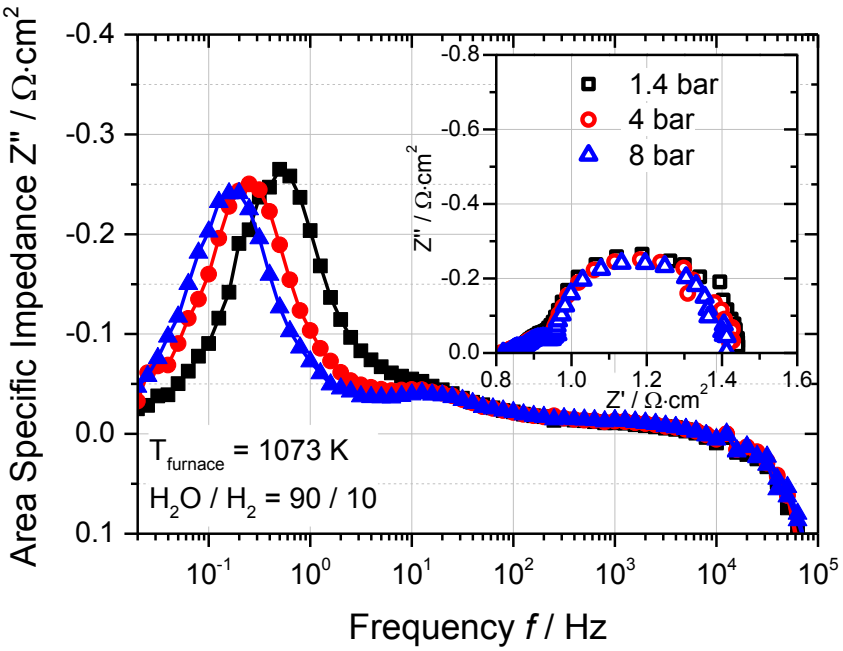

Figure 7: EIS recorded at 800 °C for 1.4, 4 and 8 bar. For each cell 1 slpm was supplied with 90 % H_2O and 10 % H_2 at the fuel electrodes. The oxygen side was flushed with 1 slpm/cell air.

Next to the lowered peak frequencies, a slight decrease of the resistance could be observed in the described low frequency part with increased operating pressure. As stated by Primdahl et al the

resistance related to gas concentration is predicted to be independent of pressure [16], [17]. The observed phenomena of a decreasing resistance in the low frequency part with increasing pressure could possibly be explained with a pressure dependent charge-transfer process of the fuel electrode located in that frequency part. Riegraf et al already observed a charge transfer to be located at very low frequencies for Ni-GDC10 electrodes [18]. With higher pressures, the resistance of charge transfer processes is decreased due to an increased concentration of reactants at active sites of the cells. Accordingly, the resistance of converting the reactants is reduced and could therefore lead to the observed decreased resistance in the low frequency part of the spectra. Furthermore, the change of the diffusion resistance may be negligible for electrolyte supported cells due to the thin electrodes and can therefore not be observed in the recorded impedance spectra [19], [20].

4.4. Ohmic resistance

Since the ohmic resistance is the most dominant part of the entire cell resistance for electrolyte supported cells, a further investigation of the temperature behavior of the ohmic part was performed. Therefore, impedance spectra were recorded for the middle cell of the stack, at 1.4 bar, OCV and in a temperature range between 650 to 850 °C. Furnace temperature was increased in 20 K steps. To ensure the stack temperature to be equal to furnace temperature at every measuring point, a dwell time of at least 90 min had to expire before EIS was performed. Out of the obtained impedance spectra, the ohmic resistance was analyzed for every temperature step. In Figure 8 the obtained experimental data for the temperature dependent ohmic resistance of the stack is shown.

(a) (b)

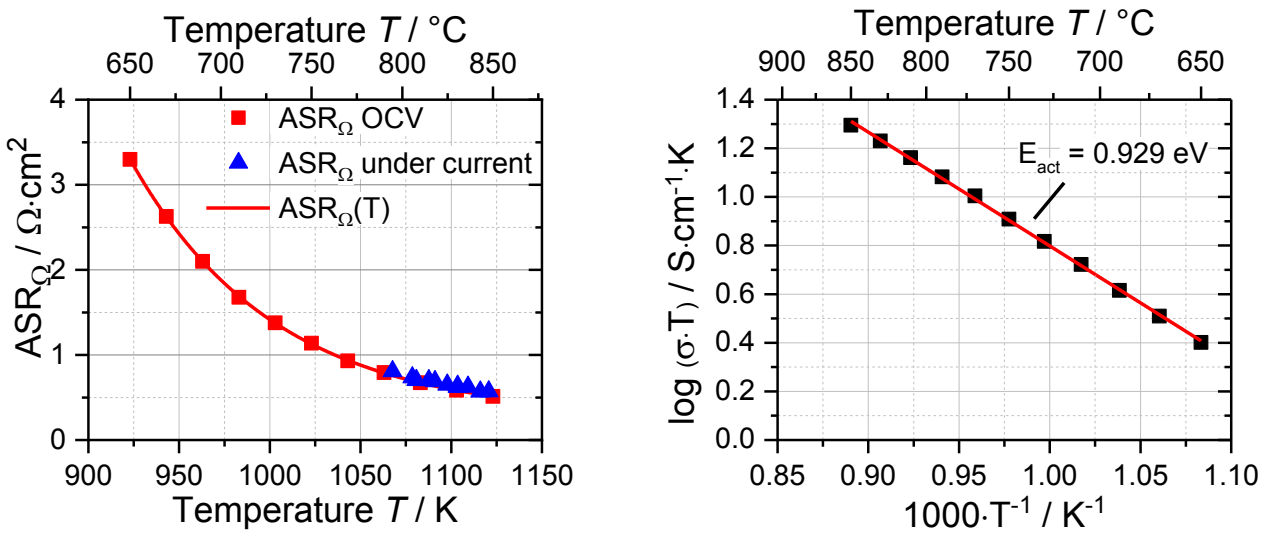

Figure 8: (a) Temperature dependency of the ohmic resistance for the middle cell of the stack. (b) Arrhenius plot for the activation energy of the ohmic resistance.

The resistance was fitted with the exponential expression $ASR_\Omega = y_0 + A \cdot \exp(B \cdot T)$. The values obtained for the fit (R^2=0.998) can be found in Table 1.

Table 1: Fit values of the temperature dependent ohmic resistance.

$ASR_\Omega = y_0 + A \cdot \exp(B \cdot T)$	
y_0 / Ω·cm^2	27.266·10^{-2}
A / Ω·cm^2	35.316·10^4
B / K^{-1}	-1.264·10^{-2}

The ohmic resistance was further determined for the middle cell of the stack from impedance measurements under load corresponding to the steady state U(i)-curves. T3 was there used as the characteristic stack temperature. In contrast to a measurement at OCV, under operating conditions the cells within the stack will have a distinct horizontal temperature profile that has a significant impact on the local ionic transport conductivity of the cells. Therefore the values of the ohmic resistance obtained out of impedance spectroscopy are an average over the cell area. As can be seen in Figure 8, these steady-state measured points nevertheless fit very well with the temperature dependent ohmic resistance curve analyzed before. This behavior indicates that the measured core

temperature of the stack is a rather good average. It can be used as the characteristic stack temperature.

With the obtained data for the temperature dependent ohmic resistance, values for an Arrhenius plot were calculated. Figure 8b shows the logarithmic scaled conductivity over the reciprocal temperature. Out of the slope of the curve, an activation energy of 0.929 eV can be calculated. This value is in good agreement with already published activation energies for YSZ as an electrolyte material [21].

With the detailed information of the temperature dependency of the ohmic resistance, the polarization resistances out of the ASR values of the dynamically recorded U(i)-curves of section 4.2 can be calculated by assuming the total ASR to consist of an ohmic (ASR_{Ω}) and a polarization part (ASR_{pol}).

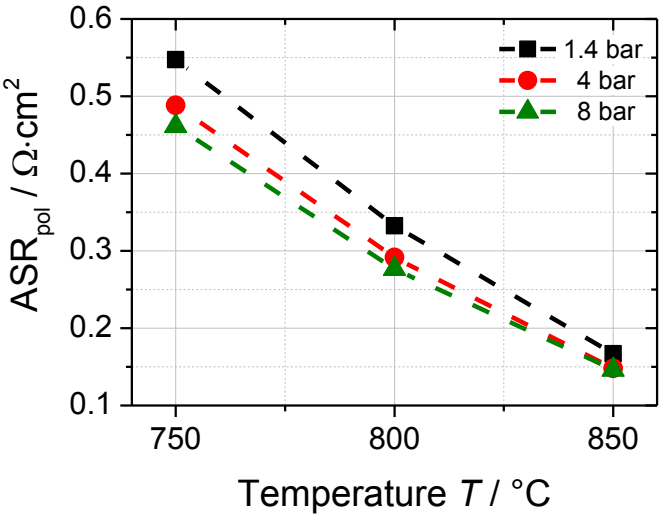

Figure 9: Analysis of the temperature and pressure dependency of the polarization resistances obtained out of the three dynamically recorded U(i)-curves shown in section 4.2.

As can be seen in Figure 9, the polarization resistances decrease with increasing temperature and increasing pressure. The largest influence of the operating pressure on the polarization resistance is found to be at the lowest experimentally performed operating temperature of 750 °C. There, the resistance is reduced by 59 mΩ·cm^2 from 1.4 to 4 bar and by 27 mΩ·cm^2 from 4 to 8 bar. In contrast, at 850 °C the resistance is merely reduced by 19 mΩ·cm^2 from 1.4 to 4 bar and by

2 mΩ·cm^2 from 4 to 8 bar. Consequently, it can be seen that at lower temperatures the pressure effect plays a more significant role. This behavior can be explained with the slower electrochemical reaction kinetics at lower temperatures and thus the higher sensitivity of the polarization resistance towards changes of the operating pressure affected activation and diffusion resistances. At higher operating temperature, reaction kinetics are inherently faster and the pressure effect on the polarization resistance is reduced. Henke et al published the pressure dependency of the activation and concentration overvoltages up to a pressure of 20 bar [5]. It was shown that these resistances are following a logarithmic behavior, i.e. the major pressure influence is found at lower pressures. Hence, it can be assumed that the shown U(i)-curves of this study would not show a significant higher pressure dependency by expanding the operating pressure to higher values.

4.5. Theoretical analysis of the ohmic resistance

In the following section a simple theoretical analysis of the ohmic resistance of a single repeating unit of a stack is introduced. To the experimentally obtained ohmic cell resistance shown in Figure 8a, several single resistances as e.g. the ion transfer through the electrolyte, the electrical resistance of the electrochemically active material (anode/cathode functional layer), the protective layers of a single repeating unit, the electrically conductive parts (Nickel mesh, interconnect, wires), contact resistances or delamination effects between the cell layers or eventually occurring oxide layers may contribute. This modeling approach was made to investigate and quantify the proportion of the ohmic resistance coming from (i) the used materials with significant resistance, (ii) the used materials without significant resistance and (iii) additional contact resistance of one repeating unit. According to equation (2), an idealized ohmic resistance can be calculated using the electrical or ionic conductivities of the individual materials of one single repeating unit of the stack.

$$ASR_{\Omega} = \frac{\delta_{ic}}{\rho^{-1}_{ic}} + \frac{\delta_{mesh}}{\rho^{-1}_{mesh}} + \frac{\delta_{fe}}{\rho^{-1}_{fe}} + \frac{2\delta_{barr}}{\rho^{-1}_{barr}} + \frac{\delta_{el}}{\rho^{-1}_{el}} + \frac{\delta_{ae}}{\rho^{-1}_{ae}} + \frac{\delta_{cl}}{\rho^{-1}_{cl}} + \frac{\delta_{crb}}{\rho^{-1}_{crb}} \quad (2)$$

Here δ stands for the thickness of the specific layer and ρ for the resistivity of the characteristic material. The resistivity of the Nickel mesh (ρ_{mesh}) as the current conductor in the fuel compartment and the stainless steel material of the interconnect (ρ_{ic}) is much lower than the one of the ceramic materials of the electrochemical cell (see Figure 10). Furthermore, the total resistivities of the materials of the fuel electrode (ρ_{fe}), the air electrode functional layer (ρ_{ae}) and the contact layer at the air side (ρ_{cl}) are generally considered to be much lower than the values for the electrolyte (ρ_{el}) or the GDC barrier layers (ρ_{barr}) between the two electrodes and the electrolyte. The barrier layer on the interconnect to prevent chromium poisoning of the air electrode (ρ_{crb}) is neglected for the presented modeling approach due to its very low thickness. Among the materials under consideration, the total resistivity of GDC is close to the same order of magnitude as the electrolyte material at the regarded operating temperature range for SOECs.

Figure 10 shows a simplified sketch of one single repeating unit and highlights the simplifications for the presented modeling approach.

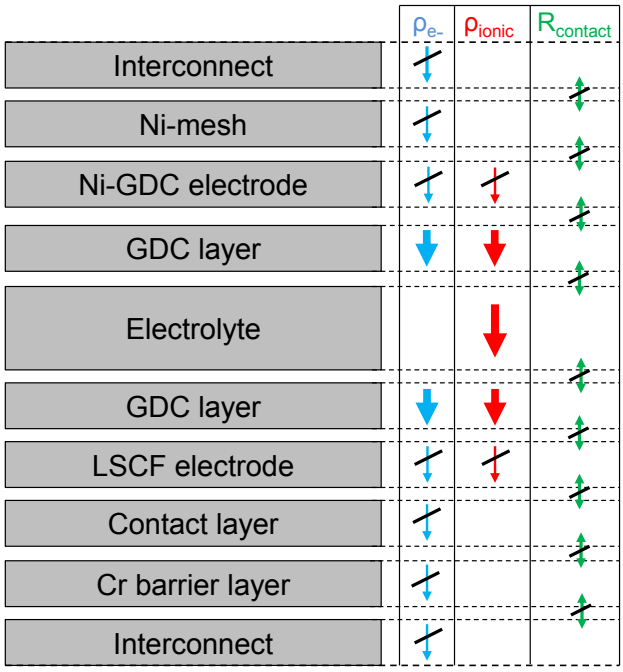

component	magnitude of ρ	
Interconnect	10^{-8} Ω·m	[22]
Nickel-mesh	10^{-7} Ω·m	[23]
Ni-GDC electrode	10^{-5} Ω·m	[24]
Electrolyte	10^{0} Ω·m	[25]
GDC barrier layer	10^{-1} Ω·m	*
LSCF electrode	10^{-5} Ω·m	[26]
Cr barrier layer	10^{-4} Ω·m	[27]
Contact layer	10^{-4} Ω·m	[28]

Figure 10: Simplified sketch of one single repeating unit of the stack. Arrows represent the electrical- (ρ_{e-}) and ionic (ρ_{ionic}) resistivities of each material and the contact resistances ($R_{contact}$) between each component. Neglected resistivities and resistances for the presented modeling approach are scored out with diagonal bars. The magnitudes of the material resistivities are shown on the right side.

* Value experimentally obtained by DLR with a pure GDC pellet in a furnace condition

Electrical- (ρ_{e-}) and ionic (ρ_{ionic}) resistivities of the different materials (i, ii) as well as the contact resistances ($R_{contact}$) between each material layer (iii) are represented by arrows. The components with very low total resistivities (<10^{-3} Ω·m) were assumed to be negligible for this modeling approach and are scored out with diagonal bars in Figure 10. Furthermore, the contact resistances between the material layers are neglected, but are assumed to have a significant influence on the overall ohmic resistance.

The temperature dependent specific conductivity, as the reciprocal value of the resistivity of the GDC material, was calculated by the following equation reported by Park et al [29].

$$\sigma^{GDC} = \frac{1.3 \cdot 10^5 \ S \cdot K \cdot cm^{-1}}{T} \cdot \exp\left(-\frac{0.7\ eV}{k \cdot T}\right) \quad (3)$$

In contrast to the dense electrolyte material, the GDC layer is very porous (ε=0.4). The porosity was taken into account via the equation reported by Wahl et al [30].

$$\sigma_\varepsilon = \sigma \cdot (1-\varepsilon)^{1.5} \quad (4)$$

Out of the conductivities for each material, the ohmic resistances were calculated with the characteristic thickness of the specific layer in the cell. The temperature dependent ohmic resistance of the 3YSZ electrolyte (data by Kerafol) and GDC material is shown in Figure 11. The temperature dependency of the resistance of the GDC material was analyzed by DLR in a furnace environment. The modeled area specific resistance of GDC and 3YSZ material is furthermore compared with the experimentally obtained results for the ohmic resistance of one single repeating unit of the characterized stack (section 4.4).

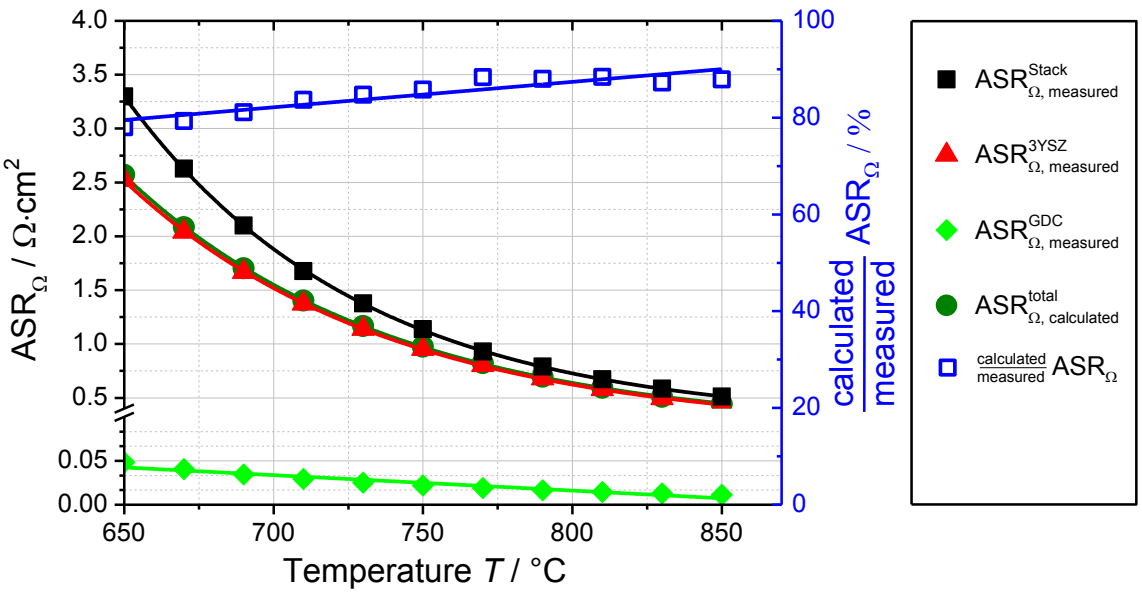

Figure 11: Comparison between the ohmic resistance of one cell of the stack (see section 4.4) and the ohmic resistance of GDC and 3YSZ material.

It can be observed that the experimentally obtained values for the ohmic resistances are higher than the calculated ones of the total ASR_Ω ($ASR^{total}_{\Omega,calculated}$). In the considered temperature range from 650 to 850 °C a deviation of 15-20 % between the modeled and the experimentally obtained ohmic resistance can be observed. This indicates a noticeable influence of one or more additional resistances in the repeating unit. Most likely this is reasoned by a poor contact between the electrochemically active cell materials and the electronic conductive parts of the repeating unit. It could therefore be a promising path to investigate the origin and reduce the additional resistance for prospective improvements. As can be seen in this study, a proportion of the ohmic resistance of 15-20 % which is not purely driven by the used material in the repeating unit reveals significant potential for an improvement of the performance of prospective stacks.

4.6. 1000 h durability test at 1.4 bar

For a durability test at 1.4 bar in steam electrolysis mode, a new stack was used. In Figure 12 the cell voltage of the middle cell of the 10-layer stack and the core temperature as a function of time at constant-current steam electrolysis is shown. The chosen gas composition for the durability test was

a mixture of 90 % H_2O with 10 % H_2 at a furnace temperature of 800 °C. Gas flows were adjusted for a steam conversion rate of 70 % at a current density of -0.5 A·cm^{-2}. At these experimental conditions the applied current density corresponded to an exothermic operation of the stack (U_{cell}>1.28 V).

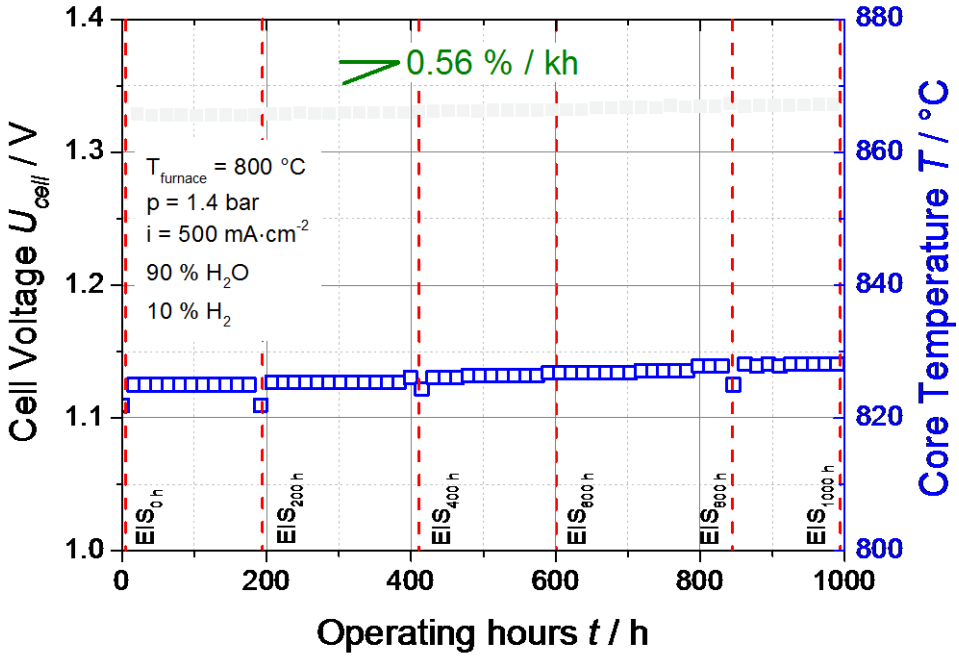

Figure 12: 1000 hours durability test on 1.4 bar, a furnace temperature of 800 °C, 90 % H_2O + 10 % H_2 with a steam conversion rate of 70 % at -0.5 A·cm^{-2}.

Within the 1000 hours durability test the voltage degradation per cell was found to be 0.008 V·kh^{-1}. This corresponds to a voltage degradation rate of 0.56 %/kh and a degradation rate of the ASR of 2.11 %/kh. Due to the increasing operating voltage during the test, core temperature increased by 3.13 K over the 1000 hours of testing time.

In order to get a deeper insight into the degradation behavior, EIS was performed every 200 hours of operating time.

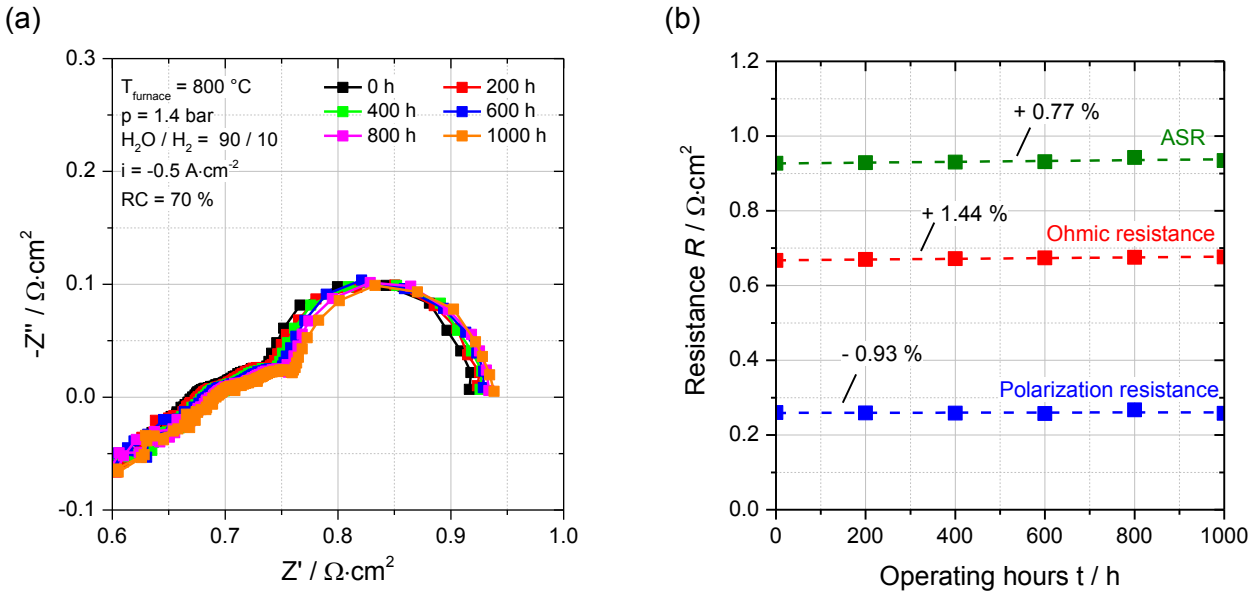

Figure 13: (a) EIS recorded at 0, 200, 400, 600, 800 and 1000 hours of operating time. (b) Change of the ohmic and polarization resistance and the total ASR over 1000 hours of operation.

As can be seen in Figure 13a, the ASR increases over the 1000 hours of operation. This behavior can be mainly attributed to an increase of the ohmic resistance. Although the stack temperature is increased due to the increase of the cell voltages, one could see the ohmic resistance of the middle cell of the stack still increases. Figure 13b shows the change of the ohmic resistance, the ASR and the polarization resistance over 1000 hours. The values for the ohmic resistance and the total ASR were obtained out of the Nyquist plots of Figure 13a. The values for the polarization resistance were obtained by subtracting the ohmic from the total resistance and were found to decrease over the 1000 hours of operation. This behavior can be attributed to the increased stack temperature and the related faster electrochemical reaction kinetics. The slight decrease of the polarization resistance points to the fact to be triggered by the increased stack temperature, so that significant microstructural changes in the thin electrodes and an impact on e.g. diffusion resistances are unlikely. Nevertheless, a detailed analysis of the cells is ongoing and will be published subsequently. Due to the increase of the core temperature by 3.13 K over the 1000 hours of operation, the temperature independent voltage degradation rate can be calculated with the information of the ohmic resistance given in section 4.4. With an increase of the characteristic

temperature by 3.13 K the ASR_{Ω} is decreased by 2.13 %. Assuming a linear change of the gas composition along the length of the cell, the theoretical voltage is reduced due to that temperature effect by 1.0 mV. As a consequence, by neglecting the change of the polarization resistance and by taking the change of the theoretical voltage into account, it leads to a slightly higher temperature independent voltage degradation rate of 0.64 %/kh.

To determine the degradation rate at higher operating pressures, long-term experiments at 4 and 8 bar will be conducted. A distinctly higher degradation rate at higher operating pressures is expected due to the possible higher mobility of Nickel with higher partial pressures of steam [31]. Furthermore, delamination effects at the air electrode could be observed due to the higher partial pressure of oxygen [32]. The results will be presented in a following publication by the authors.

5. Conclusion

In this work two commercially available SOC stacks were used for an electrochemical characterization in steam electrolysis mode. The stacks consist of 10 planar electrolyte supported cells. SOC test results for steady-state and dynamic recorded characterizations were demonstrated under elevated operating pressures up to 8 bar.

The results show that the cell voltages increase with the increase of pressure as predicted by the Nernst equation. Furthermore a slight positive influence on the performance of the stack could be observed in the dynamically and stationary recorded U(i)-curves as well as in the obtained impedance spectra. Due to the dominant and pressure independent ohmic resistance combined with the thin electrodes and the high operating temperature of the electrolyte supported cells, the decrease in the activation and diffusion resistances is low.

Impedance data showed a high resistance at low frequencies which is normally attributed to gas concentration impedance. The peak frequency of this low frequency process decreased with increasing operating pressure. Furthermore the resistance at this low frequency process was slightly decreased. Pure gas concentration impedance should not be affected by pressure [10]. This

behavior could possibly be explained with a pressure dependent charge transfer process on the fuel electrode which was already found at quite low frequencies for Ni-GDC electrodes in literature [18]. The most dominant part of the impedance spectra was found to be the ohmic resistance which was closely investigated within a temperature range from 650 °C to 860 °C and was fitted with an exponential expression. A highly simplified model was set up to analyze the ohmic resistance part of the electrolyte supported cells. A comparison between the experimentally obtained data for the ohmic resistance and the values of GDC and 3YSZ material showed a deviation of 15-20 % over the considered temperature range (650-860 °C). This could be reasoned by a poor contact between the electrochemically active cell materials and the electrical conductive parts or by eventually formed oxide layers during the operation on the metal-based components of the repeating unit. The study showed that the proportion of the ohmic resistance which is not purely driven by the used material in the repeating unit reveals significant potential for an improvement of the performance of prospective stack developments, especially because the ohmic resistance is the major part of entire cell resistance for electrolyte supported cells.

The second stack in this study was used for a long term degradation test at 1.4 bar and a steam conversion rate of 70 % at 0.5 $A \cdot cm^{-2}$ over 1000 hours. These conditions lead to an exothermic behavior of the stack (U>1.28 V). A voltage increase of 8 mV was observed over the 1000 hours of operation which corresponds to a voltage degradation rate of 0.56 %/kh. Due to the voltage driven parallel increase of the stack temperature, the actual degradation rate was calculated to be slightly higher. With the performed detailed analysis of the temperature dependency of the ohmic resistance of the stack, the voltage degradation rate was corrected on account of the temperature increase. The actual voltage degradation rate was found to be 0.64 %/kh.

Acknowledgement

This work was financially supported by the project “pressurized high temperature electrolysis” (DruHEly) of the Federal Ministry of Economic Affairs and Energy (BMWi, funding code 03ET6051). The responsibility for the report's contents lies with the authors.

Supported by:

on the basis of a decision
by the German Bundestag

Nomenclature and abbreviations

Abbreviations

SOC	Solid Oxide Cell
SOEC	Solid Oxide Electrolysis Cell
HTSE	High Temperature Steam Electrolysis
EIS	Electrochemical Impedance Spectroscopy
LSCF	Lanthanum Strontium Cobalt Ferrite
YSZ	Yttria-stabilized zirconia
GDC	Gadolinium-doped ceria
Ni	Nickel
OCV	Open Circuit Voltage
CSTR	Continuous Stirred-Tank Reactor

Latin letters

U	Voltage, V
i	Current density, $A \cdot cm^{-2}$
R	Gas constant, $J \cdot mol^{-1}\ K^{-1}$
z	Number of electrons, -
F	Faraday constant = 96485.33, C/mol
slpm	Standard liters per minute, $l \cdot min^{-1}$
T	Temperature, °C/K
RC	Reactant Conversion, %
p	Pressure, bar
ASR	Area Specific Resistance, $\Omega \cdot m^2$

Greek letters

ρ	Resistivity, Ω·m
σ	Conductivity, $S \cdot m^{-1}$
ε	Porosity, %

1

2 *Subscripts*

tot	Total
pol	Polarization
ic	Interconnect
mesh	Mesh
fe	Fuel electrode
barr	Barrier Layer
el	Electrolyte
ae	Air Electrode
cl	Contact Layer
crb	Chromium barrier layer

3

4

Literature

[1] V. N. Nguyen, Q. Fang, U. Packbier, and L. Blum, “Long-term tests of a Jülich planar short stack with reversible solid oxide cells in both fuel cell and electrolysis modes,” *Int. J. Hydrogen Energy*, vol. 38, no. 11, pp. 4281–4290, 2013.

[2] T. N. Vezirolu and F. Barbir, “Hydrogen: the wonder fuel,” *Int. J. Hydrogen Energy*, vol. 17, no. 6, pp. 391–404, 1992.

[3] P. P. Edwards, V. L. Kuznetsov, W. I. F. David, and N. P. Brandon, “Hydrogen and fuel cells: Towards a sustainable energy future,” *Energy Policy*, vol. 36, no. 12, pp. 4356–4362, 2008.

[4] S. H. Jensen, C. Graves, M. Chen, J. B. Hansen, and X. Sun, “Characterization of a Planar Solid Oxide Cell Stack Operated at Elevated Pressure,” *J. Electrochem. Soc.*, vol. 163, no. 14, pp. F1596–F1604, 2016.

[5] M. Henke, C. Willich, J. Kallo, and K. A. Friedrich, “Theoretical study on pressurized operation of solid oxide electrolysis cells,” *Int. J. Hydrogen Energy*, vol. 39, pp. 12434–12439, 2014.

[6] L. Bernadet, G. Gousseau, A. Chatroux, J. Laurencin, F. Mauvy, and M. Reytier, “Influence of pressure on solid oxide electrolysis cells investigated by experimental and modeling approach,” *Int. J. Hydrogen Energy*, vol. 40, no. 38, pp. 12918–12928, 2015.

[7] X. Sun, M. Chen, S. H. Jensen, S. D. Ebbesen, C. Graves, and M. Mogens, “Thermodynamic analysis of synthetic hydrocarbon fuel production in PSOEC,” *Int. J. Hydrogen Energy*, vol. 37, pp. 17101–17110, 2012.

[8] A. Momma, K. Takano, Y. Tanaka, T. Kato, and A. Yamamoto, “Experimental Investigation of the Effect of Operating Pressure on the Performance of SOFC and SOEC,” in *ECS Transaction*, 2013, vol. 57, pp. 699–708.

[9] J. E. O ’brien, C. M. Stoots, J. S. Herring, M. G. Mckellar, E. A. Harvego, M. S. Sohal, and K. G. Condie, “High Temperature Electrolysis for Hydrogen Production from Nuclear Energy – Technology Summary,” 2010.

[10] S. H. Jensen, X. Sun, S. D. Ebbesen, and M. Chen, “Pressurized Operation of a Planar Solid

Oxide Cell Stack," *Fuel Cells*, vol. 16, no. 2, pp. 205–218, 2016.

[11] M. Riedel, M. P. Heddrich, and K. A. Friedrich, "1st International Conference on Electrolysis," in *Book of Abstracts*, 2017, p. 71.

[12] S. Seidler, M. Henke, J. Kallo, W. G. Bessler, U. Maier, and K. A. Friedrich, "Pressurized solid oxide fuel cells: Experimental studies and modeling," in *Journal of Power Sources*, 2011, vol. 196, no. 17, pp. 7195–7202.

[13] S. Santhanam, M. P. Heddrich, M. Riedel, and K. A. Friedrich, "Theoretical and experimental study of Reversible Solid Oxide Cell (r-SOC) systems for energy storage," *Energy*, vol. 141, pp. 202–214, 2017.

[14] L. Bernadet, G. Gousseau, A. Chatroux, J. Laurencin, F. Mauvy, and M. Reytier, "Assessment of Pressure Effects on High Temperature Steam Electrolysis Based on Solid Oxide Technology," *ECS Trans.*, vol. 68, no. 1, pp. 3369–3378, 2015.

[15] X. Sun, A. D. Bonaccorso, C. Graves, S. D. Ebbesen, S. H. Jensen, A. Hagen, P. Holtappels, P. V. Hendriksen, and M. B. Mogensen, "Performance characterization of solid oxide cells under high pressure," in *Fuel Cells*, 2015, vol. 15, no. 5, pp. 697–702.

[16] S. Primdahl, "Gas Conversion Impedance: A Test Geometry Effect in Characterization of Solid Oxide Fuel Cell Anodes," *J. Electrochem. Soc.*, vol. 145, no. 7, p. 2431, 1998.

[17] S. Primdahl, "Gas Diffusion Impedance in Characterization of Solid Oxide Fuel Cell Anodes," *J. Electrochem. Soc.*, vol. 146, no. 8, p. 2827, 1999.

[18] M. Riegraf, V. Yurkiv, R. Costa, G. Schiller, and K. A. Friedrich, "Evaluation of the Effect of Sulfur on the Performance of Nickel/Gadolinium-Doped Ceria Based Solid Oxide Fuel Cell Anodes," *ChemSusChem*, vol. 10, no. 3, pp. 587–599, 2017.

[19] W. G. Bessler and S. Gewies, "Gas Concentration Impedance of Solid Oxide Fuel Cell Anodes," *J. Electrochem. Soc.*, vol. 154, pp. 548–559, 2007.

[20] H. Zhu and R. J. Kee, "A general mathematical model for analyzing the performance of fuel-cell membrane-electrode assemblies," *J. Power Sources*, vol. 117, pp. 61–74, 2003.

[21] J. Nielsen and J. Hjelm, "Impedance of SOFC electrodes: A review and a comprehensive

case study on the impedance of LSM:YSZ cathodes," *Electrochim. Acta*, vol. 115, pp. 31–45, 2014.

[22] Z. G. Yang, D. M. Paxton, K. S. Weil, J. W. Stevenson, and P. Singh, "Materials Properties Database for Selection of High-Temperature Alloys and Concepts of Alloy Design for SOFC Applications," 2002.

[23] L. Abadlia, F. Gasser, K. Khalouk, M. Mayoufi, and J. G. Gasser, "New experimental methodology, setup and LabView program for accurate absolute thermoelectric power and electrical resistivity measurements between 25 and 1600 K: Application to pure copper, platinum, tungsten, and nickel at very high temperatures," *Rev. Sci. Instrum.*, 2014.

[24] A. Infortuna, A. S. Harvey, U. P. Muecke, and L. J. Gauckler, "Nanoporous Ni–Ce0.8Gd0.2O1.9−x thin film cermet SOFC anodes prepared by pulsed laser deposition," *Phys. Chem. Chem. Phys.*, 2009.

[25] D. J. L. Brett, A. Atkinson, N. P. Brandon, and S. J. Skinner, "Intermediate temperature solid oxide fuel cells," *Chem. Soc. Rev.*, 2008.

[26] K. Yashiro, I. Nakano, M. Kuhn, S. Hashimoto, K. Sato, and J. Miuzusaki, "Electrical conductivity and oxygen diffusivity of perovskite-type solid solution LSCF," in *219th ESC Meeting*, 2011, p. #739.

[27] X. Chen, P. Y. Hou, C. P. Jacobson, S. J. Visco, and L. C. De Jonghe, "Protective coating on stainless steel interconnect for SOFCs: Oxidation kinetics and electrical properties," *Solid State Ionics*, vol. 176, no. 5–6, pp. 425–433, 2005.

[28] E. Ivers-Tiffeé, A. Weber, and D. Herbstritt, "Materials and technologies for SOFC-components," *J. Eur. Ceram. Soc.*, vol. 21, pp. 1805–1811, 2001.

[29] S. H. Park and H. I. Yoo, "Defect-chemical role of Mn in Gd-doped CeO2," *Solid State Ionics*, vol. 176, no. 15–16, pp. 1485–1490, 2005.

[30] S. Wahl, A. G. Segarra, P. Horstmann, M. Carré, W. G. Bessler, F. Lapicque, and K. A. Friedrich, "Modeling of a thermally integrated 10 kW planar solid oxide fuel cell system with anode offgas recycling and internal reforming by discretization in flow direction," *J. Power*

Sources, vol. 279, pp. 656–666, 2015.

[31] M. B. Mogensen, A. Hauch, X. Sun, M. Chen, Y. Tao, S. D. Ebbesen, K. V. Hansen, and P. V. Hendriksen, “Relation Between Ni Particle Shape Change and Ni Migration in Ni–YSZ Electrodes – a Hypothesis,” *Fuel Cells*, vol. 17, no. 4, pp. 434–441, 2017.

[32] P. Moçoteguy and A. Brisse, “A review and comprehensive analysis of degradation mechanisms of solid oxide electrolysis cells,” *Int. J. Hydrogen Energy*, vol. 38, no. 36, pp. 15887–15902, 2013.